



1-28-2019

On the Remote Estimation of *Ulva Prolifera* Areal Coverage and Biomass

Lianbo Hu
University of North Dakota

Kan Zeng

Chuanmin Hu

Ming-Xia He

[How does access to this work benefit you? Let us know!](#)

Follow this and additional works at: <https://commons.und.edu/essp-fac>

Recommended Citation

Lianbo Hu, Kan Zeng, Chuanmin Hu, et al.. "On the Remote Estimation of *Ulva Prolifera* Areal Coverage and Biomass" (2019). *Earth System Science and Policy Faculty Publications*. 9.
<https://commons.und.edu/essp-fac/9>

This Article is brought to you for free and open access by the Department of Earth System Science and Policy at UND Scholarly Commons. It has been accepted for inclusion in Earth System Science and Policy Faculty Publications by an authorized administrator of UND Scholarly Commons. For more information, please contact und.commons@library.und.edu.



On the remote estimation of *Ulva prolifera* areal coverage and biomass

Lianbo Hu^{a,b,c,*}, Kan Zeng^{a,b}, Chuanmin Hu^d, Ming-Xia He^a

^a Ocean Remote Sensing Institute, Ocean University of China, 5 Yushan Road, Qingdao 266003, China

^b Laboratory for Regional Oceanography and Numerical Modeling, Qingdao National Laboratory for Marine Science and Technology, 1 Wenhai Road, Qingdao 266200, China

^c Department of Earth System Science and Policy, University of North Dakota, 4149 University Avenue, Grand Forks, ND 58202, USA

^d College of Marine Science, University of South Florida, 140 Seventh Avenue South, St. Petersburg, FL 33701, USA



ARTICLE INFO

Keywords:

Ulva prolifera
Remote sensing
Areal coverage
Biomass

ABSTRACT

Since the outbreak of a large-scale *Ulva prolifera* bloom in the Yellow Sea during the Qingdao Olympic Sailing Competition in summer 2008, *Ulva* blooms have been a marine hazard every summer. Accurate and timely information on *Ulva* areal coverage and biomass is of critical importance for governmental responses, decision making, and field studies. Previous studies have shown that satellite remote sensing is the most effective method for this purpose, yet *Ulva* areal coverage has been estimated in different ways with significantly different results. The objective of this paper is to determine the lower and upper bounds (T_0 and T_1) of algae-containing pixels in Floating Algae Index images with an objective method that accurately estimates the *Ulva* areal coverage in individual images, and then converts coverage to biomass using a previously established conversion equation. First, a seawater background image, FAI_{sw} , is constructed to determine T_0 , which varies for different algae patches. Then, T_1 is determined from water tank and in situ measurements as well as radiative transfer simulations to account for different sensor configurations, solar/viewing geometry, and atmospheric conditions. Such determined T_1 for MODIS 250-m resolution data is validated using concurrent and collocated 2-m resolution WorldView-2 data. Finally, *Ulva* areal coverage derived from MODIS data using this method are compared with those from the high-resolution data (OLI/Landsat, WFV/GaoFen-1), with a mean relative difference of 9.6%. Furthermore, an analysis of 17 same-day MODIS/Terra and MODIS/Aqua image pairs shows that large viewing angles, atmospheric turbidity, and sunglint can lead to an underestimation of *Ulva* coverage of up to 45% under extreme conditions.

1. Introduction

Since the outbreak of a large-scale green tide in the Yellow Sea (YS) during the Qingdao Olympic Sailing Competition in summer 2008, green tides have been a marine hazard every summer in China (China SOA, 2016). The dominated species of the green tides in the YS was identified as *Ulva prolifera* based on morphology observations and molecular analysis conducted on samples from coastal waters off Qingdao and from the YS (Zhang et al., 2008; Wang et al., 2008; Leliaert et al., 2009; Wang et al., 2015). It is generally accepted that *Ulva* blooms originate from the Subei Shoal, as evidenced by satellite remote sensing (Hu and He, 2008; Liu et al., 2009), numerical model simulations (Lee et al., 2011), or in situ experiments (Liu et al., 2010; Huo et al., 2013). Although it has been proposed that local aquaculture ponds are possible bloom origins (Pang et al., 2010; F. Liu et al., 2013), there is a general consensus that *Porphyra yezoensis* aquaculture in the

Subei Shoal is most likely the ‘seed’ source of the *Ulva* blooms (Liu et al., 2009; Liu et al., 2010; Hu et al., 2010c; D. Liu et al., 2013; Hu et al., 2014; Liu et al., 2015; Wang et al., 2015; Zhang et al., 2017). *Ulva* could grow with *P. yezoensis* on aquaculture rafts and then be discarded by farmers when *P. yezoensis* is harvested and rafts are cleaned in April. The disposed fragments of *Ulva* may drift to offshore waters and grow rapidly, forming large-scale blooms in the YS (Liu et al., 2016).

Satellite remote sensing is one of the most effective tools for *Ulva* bloom monitoring. Since 2008, MODIS data covering the region twice a day have been widely used for bloom monitoring with many algae indices, including the Normalized Difference Vegetation Index (NDVI) (Hu and He, 2008; Cui et al., 2012), Normalized Difference Algae Index (NDAI) (Shi and Wang, 2009), Floating Algae Index (FAI) (Hu, 2009; Hu et al., 2010c; He et al., 2011; Xu et al., 2014a; Hu et al., 2017), Scaled Algae Index (SAI) (Keesing et al., 2011; Garcia et al., 2013) and Virtual-Baseline Floating macroAlgae Height (VB-FAH) (Xing and Hu,

* Corresponding author at: Ocean Remote Sensing Institute, Ocean University of China, 5 Yushan Road, Qingdao 266003, China.

E-mail address: hulb@ouc.edu.cn (L. Hu).

<https://doi.org/10.1016/j.rse.2019.01.014>

Received 1 July 2018; Received in revised form 9 January 2019; Accepted 11 January 2019

Available online 28 January 2019

0034-4257/© 2019 The Authors. Published by Elsevier Inc. This is an open access article under the CC BY license

(<http://creativecommons.org/licenses/by/4.0/>).

Table 1

Statistics of *Ulva* areal coverage in the YS on 30 May 2008 using cloud-free MODIS data, based on published literature. The symbol ‘-’ indicates that T_1 is not used in the study because each algae-containing pixel is assumed to have complete (i.e., 100%) algae coverage.

Coverage (km ²)	Index	Sub-pixel coverage	Thresholds		Literature
			T_0	T_1	
1200	NDVI	No	Fixed		Liu et al. (2009)
2240	NDAI	No	Fixed	–	Shi and Wang (2009)
3475	SAI(NDVI)	No	SAI _{sw}	–	Keesing et al. (2011)
1200	NDVI	No	Fixed	–	Xing et al. (2015)
1500	FAI	Yes	0	0.02	Xu et al. (2014a)
234	FAI	Yes	0.0025	0.176	Qi et al. (2016)
378–417	SAI (NDVI)	Yes	SAI _{sw}	SAI _{max}	Garcia et al. (2013)

2016). However, the reported *Ulva* areal coverage data are significantly different among the published studies; for example, there are large discrepancies (p-value = 0.03 of *t*-test statistic) in these coverage estimates for the bloom event of 30 May 2008 (Table 1) when the estimate from Garcia et al.'s is used as the expected value. These discrepancies can represent a difference of up to 15 times, which may be due to a number of factors, including differences in (1) the indices used, (2) the treatment of algae-containing pixels (i.e., whether to consider sub-pixel coverage), (3) and the thresholds used in the unmixing model if sub-pixel coverage is considered. Obviously, because most algae-containing pixels in MODIS imagery are partially covered by algae (Hu et al., 2017) due to the relatively large pixel size (> 250 m), a reliable model to unmix the sub-pixel coverage is required to reduce uncertainties in the areal coverage estimates and in subsequent biomass estimates. The question then becomes what index to use and how to select the thresholds when unmixing pixels.

Among the various indexes used to detect and quantify *Ulva* blooms, FAI is based on the linear subtraction of a spectral baseline to quantify the vegetation red-edge reflectance (i.e., elevated reflectance in near infrared) and is thus relatively insensitive to changes in sun/sensor viewing geometry and atmospheric conditions (Hu, 2009). More importantly, the linear subtraction design of FAI makes it possible to estimate sub-pixel coverage using a linear unmixing model, thereby suitable to accurately quantify the areal coverage of blooms (Hu et al., 2010c). Recently, *Ulva* biomass was remotely estimated using MODIS measurements, where a model was used to convert FAI to biomass (Hu et al., 2017). Moreover, FAI has been widely used to map other macroalgae blooms (e.g., *Sargassum* blooms in the West Atlantic) in open-ocean waters (Wang and Hu, 2016; Hu et al., 2016a; Hu et al., 2016b) and cyanobacteria blooms in Lake Taihu of China (Hu et al., 2010b; Duan et al., 2015; Liang et al., 2017) and the West Florida Shelf (Hu et al., 2010a).

Thus, FAI may be a good choice for the linear unmixing of mixed pixels. However, the difficulty still remains on how to determine the lower and upper bounds of thresholds, T_0 and T_1 , respectively, to represent 0% and 100% algae coverage within a pixel. Using statistics of 430 MODIS images of cyanobacteria blooms in Lake Taihu, Hu et al. (2010b) determined T_0 to be 0.004 (dimensionless), and this value was then applied to time series MODIS data to estimate *Ulva* areal coverage (Hu et al., 2010c; Xu et al., 2014a). A fixed T_0 is easy to implement in image processing, yet T_0 can vary with seawater optical properties (e.g., turbidity) and atmospheric conditions (e.g., haze or sunglint) (Keesing et al., 2011; Garcia et al., 2013). On the other hand, the North China Sea Marine Forecasting Center of State Ocean Administration (NCSMFC/SOA) of China utilized MODIS NDVI in operational *Ulva* bloom monitoring with a T_0 threshold between [–1.5,0] selected by an experienced human analyst (Zhong et al., 2013; Ding et al., 2015). Garcia et al. (2013) developed the SAI method by subtracting the median value in a moving kernel window to scale the NDVI image to the local seawater background, where clear seawater areas close to the algae patches were manually selected to statistically derive T_0 . Qi et al.

(2016) varied T_0 in each MODIS image until the delineated algae slicks agreed with visual inspection. Because of the sensitivity of T_0 to the background ocean turbidity and because of the extremely high turbidity in the shallow Subei Shoal, the pixels over Subei Shoal were masked in Qi et al. (2016). Similarly, in Wang and Hu (2016), although large-scale variations in seawater background FAI were addressed through the use of 4th-order surface fitting, the method could not be applied to sudden changes in seawater background FAI such as those from Subei Shoal or very turbid coastal waters. These methods to determine T_0 are all subject to some degree of uncertainties when the seawater background FAI change rapidly, and are relatively difficult to implement for operational use. Likewise, the selection of T_1 using a maximum SAI value from individual images (Garcia et al., 2013) is subject to uncertainties because, during early stage of *Ulva* blooms, there may be no pixels completely covered by *Ulva*, and in later bloom stages, the maximum SAI used to represent T_1 could be an overestimate. In this case, the near-infrared reflectance still increases with increasing biomass density but at a lower rate after a certain threshold (Hu et al., 2017), leading to $FAI > T_1$. The use of variable T_1 values across images may also make the derived *Ulva* areal coverage inconsistent among images.

Clearly, once FAI is selected as the index to detect and quantify *Ulva* for the reasons mentioned above, the key technical challenge is the determination of T_0 and T_1 . The objective of this study is to develop an objective method to determine these two values, with the ultimate goal of accurately estimating *Ulva* areal coverage and biomass from satellite measurements. Specifically, a seawater background image, FAI_{sw}, is reconstructed to accurately determine T_0 , where most perturbation factors (variable turbidity, aerosols, geometry, and sun glint) are accounted for via the use of a corrected FAI image (cFAI), which is derived as the difference between the original FAI image and the seawater background image. The FAI_{sw} image not only minimizes impacts of observing conditions but also makes it possible to implement this method for operational monitoring without manual intervention. Furthermore, based on water tank and in situ experiments (Hu et al., 2017), T_1 for different sensors under different geometries and aerosols is determined and validated with very high spatial resolution WorldView-2 data (2.0 m). The new method is then used to estimate *Ulva* areal coverage from MODIS, and compared with concurrent high spatial resolution OLI/Landsat (30 m) and WFV/GaoFen-1(16 m) estimates. Finally, the impacts of satellite sensor viewing angles, aerosols, and sunglint on the derived *Ulva* areal coverage data are discussed using 17 pairs of MODIS/Terra (MODIST) and MODIS/Aqua (MODISA) images acquired in the same day.

2. Satellite data

2.1. MODIS data

MODIST and MODISA Level-0 data over the YS between May and August in each year were obtained from the NASA Godard Space Flight Center (<https://oceancolor.gsfc.nasa.gov>), and then processed to

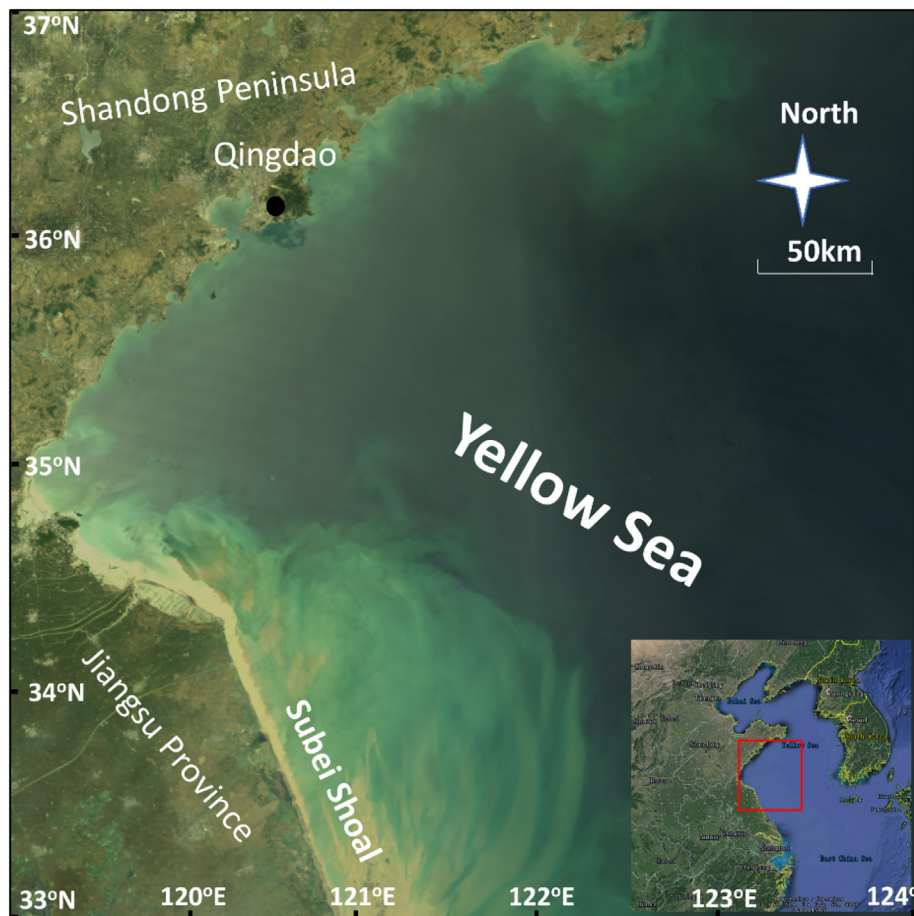


Fig. 1. Study area of the YS, bounded by 119°–124°E and 33°–37°N. The background image is the MODIS/Terra RGB image acquired on 31 May 2008. The Subei Shoal shows an extensive sediment plume.

generate Rayleigh-corrected reflectance (R_{rc} , dimensionless) data using the SeaDAS software package (Version 7.4). MODIS R_{rc} data at 469, 555, 645, 859, and 1240 nm and the sensor viewing zenith angle (VZA, degrees) were resampled at 250-m resolution and mapped to a UTM projection (Zone = 51) for the YS area (33°–37°N, 119°–124°E, Fig. 1). MODIS true-color Red-Green-Blue images (R:645 nm, G:555 nm and B:469 nm) and false-color RGB images (R:645 nm, G:859 nm and B:469 nm) were generated for visualization. For each pixel, the MODIS FAI was derived as (Hu, 2009):

$$FAI = R_{rc,NIR} - R'_{rc,NIR}$$

$$R'_{rc,NIR} = R_{rc,RED} + (R_{rc,SWIR} - R_{rc,RED}) \frac{\lambda_{NIR} - \lambda_{RED}}{\lambda_{SWIR} - \lambda_{RED}} \quad (1)$$

where the subscripts represent MODIS wavelengths as $\lambda_{RED} = 645$ nm, $\lambda_{NIR} = 859$ nm, and $\lambda_{SWIR} = 1240$ nm. For other sensors, these wavelengths can be adjusted accordingly.

2.2. OLI/Landsat-8 data

Landsat-8 was launched on 11 February 2013 carrying the OLI sensor, which measures the upwelling radiance at a nominal resolution of 30 m with 8 bands in the visible, NIR and SWIR spectral regions. OLI Level 1 data between May and August covering the study area were obtained from the USGS (<https://earthexplorer.usgs.gov/>). These radiometrically calibrated total radiance data were mapped to a UTM projection (Storey et al., 2014). OLI offers higher signal-to-noise ratios (SNR) than its predecessors TM and ETM+ (Vanhellemont and Ruddick, 2014). The total radiance was used to generate R_{rc} data using the 6S radiative transfer software (Vermote et al., 1997), and this data

was then used to derive the OLI FAI images using Eq. (1) with OLI Bands 4 (655 nm), 5 (865 nm) and 6 (1610 nm).

2.3. WFV/GaoFen-1 data

GaoFen-1 (GF-1) Level-1A data between May and August were acquired from the Chinese Center for Resources Satellite Data and Application (CRESDA) (<http://www.cresda.com/CN/index.shtml>). The GF-1 satellite was launched in April 2013 and equipped with four Wide Field of View (WFV) multi-spectral CCD (three in visible and one in NIR) with VZAs ranging from 0° to 24° for two close-nadir cameras and 24° to 40° for two off-nadir cameras (Feng et al., 2016). The spatial resolution of WFV/GF-1 is approximately 16 m at nadir, and the swath width is 800 km (Xu et al., 2014b). These resolution and coverage are appropriate to validate concurrent MODIS observations. Similar to OLI processing, the Level-1A data were calibrated to total radiance with the calibration data acquired from CRESDA, and then processed to generate R_{rc} data using the 6S radiative transfer simulation software (Vermote et al., 1997) and mapped to a UTM projection (Zone = 51) using the ENVI software. Because WFV is not equipped with a SWIR band, FAI could not be derived. Therefore, the Difference Vegetation Index (DVI) (Tucker, 1979) was estimated as

$$DVI = R_{rc,NIR} - R_{rc,RED} \quad (2)$$

2.4. WorldView-2 data

A WorldView-2 (WV-2) sub-scene (5 km × 5 km, centered at 36.650°N, 122.741°E) containing many algae patches in the YS was

acquired on 23 June 2012 from DigitalGlobe. WV-2 has eight bands in the visible and NIR with a spatial resolution of ~2.0 m. The image was mapped to the same UTM projection (Zone = 51). DN values of the WV-2 data were processed to total radiance with the corresponding metadata file (Updike and Comp, 2010) and then processed to R_{rc} and DVI (660 nm and 830 nm) using the same methods as described above for WFV/GF-1 data.

3. Method to determine *Ulva* areal coverage and biomass

For a certain region, *Ulva* areal coverage and biomass can be expressed as:

$$S = \sum_{i=1}^n \alpha_i S_{\text{pixel}} \quad (3)$$

$$T = S \sigma_0$$

where S is the *Ulva* areal coverage in km^2 ; S_{pixel} is the pixel size (for MODIS $S_{\text{pixel}} = 0.0625 \text{ km}^2$); α_i is *Ulva* areal density (from 0.0 to 1.0) in pixel i ; n is the number of algae-containing pixels, T is the total biomass in kg or metric tons, and σ_0 (kg m^{-2}) is a calibration constant determined from water tank and in situ experiments.

An algae-containing pixel in the satellite image can be considered to be composed of algae and seawater, with surface coverage values of α and $1 - \alpha$, respectively. Then, we have:

$$R_{rc, \text{pixel}} = \alpha R_{rc, \text{algae}} + (1 - \alpha) R_{rc, \text{sw}} \quad (4)$$

Because FAI is linear in the R_{rc} space, we have:

$$FAI_{\text{pixel}} = \alpha FAI_{\text{algae}} + (1 - \alpha) FAI_{\text{sw}} \quad (5)$$

where FAI_{algae} is the FAI value of pure *Ulva* (T_1), and FAI_{sw} is the FAI value of local seawater (T_0).

Thus, α can be derived as:

$$\alpha = \frac{FAI_{\text{pixel}} - FAI_{\text{sw}}}{FAI_{\text{algae}} - FAI_{\text{sw}}} = \frac{cFAI_{\text{pixel}}}{cFAI_{\text{algae}}} \quad (6)$$

where $cFAI$ indicates the corrected FAI value after scaling to (i.e., subtracting) FAI_{sw} . The following sections will describe in detail how to reconstruct the FAI_{sw} seawater background image.

3.1. Reconstruction of the seawater background image (FAI_{sw})

FAI removes most effects of atmospheric perturbation, but the FAI magnitude is still influenced by suspended sediments in turbid waters, atmospheric turbidity, and sunglint. For example, in the Subei Shoal, an abandoned Yellow River subaqueous delta (Fig. 1), the suspended particulate matter (SPM) concentration can reach 300 mg/L in April (Shen et al., 2014). Such high SPM concentrations elevate R_{rc} in the red band, leading to lower FAI values (purple area in Fig. 2a) (Hu et al., 2010b). On the other hand, MODIS images over the YS are frequently “contaminated” by atmospheric turbidity (e.g., high aerosol loading or haze) and sunglint. The disproportionately elevated R_{rc} in the red, NIR and SWIR bands lead to lower FAI values with increasing atmospheric turbidity and higher FAI values with increasing sunglint. Such variability in FAI/NDVI values of seawater within a MODIS image has been illustrated clearly in the bimodal characteristic from the histogram analysis of two seawater areas w/ and w/o sunglint (Garcia et al., 2013). When extensive turbid waters (purple area in Fig. 2a) are taken into account, the histogram of FAI values of seawater will demonstrate a multimodal distribution (Fig. 3), making it more difficult to apply a global T_0 to distinguish *Ulva* from seawater background in the image. Therefore, deriving an accurate T_0 image (where T_0 may vary across the image) instead of a global T_0 to serve as the background (FAI_{sw}) is the ideal way to address these problems. The entire process of reconstructing a seawater FAI_{sw} background image is summarized in the flowchart in Fig. 4. Specifically, after deriving corrected FAI gradient

image (cG_{FAI}) from the MODIS FAI gradient image (G_{FAI}) and MODIS $R_{rc,645}$ gradient image (G_{R645}), the threshold T_{cG} is applied to the cG_{FAI} image to classify pixels as algae-free seawater pixels ($\leq T_{cG}$) and candidate pixels ($> T_{cG}$). The latter may include algae-containing pixels and neighboring seawater pixels. Then, a variable-window method is applied to each candidate pixel to further classify whether the candidate pixel is a seawater or algae-containing pixel. The following subsections will describe the details of the corrected FAI gradient image, threshold T_{cG} , and the variable-window method.

3.1.1. Corrected FAI gradient image (cG_{FAI})

The first step is to construct a corrected FAI gradient image (cG_{FAI}). FAI values of algae-containing pixels vary in space due to patchiness, while FAI values of algae-free seawater pixels are more homogeneous. The pixel gradient magnitude is defined as:

$$\nabla y_i = \sqrt{\frac{1}{8} \sum_{j=1}^8 \left(\frac{y_i - y_j}{x_{ij}} \right)^2}, j \neq i \quad (7)$$

where ∇y_i indicates the gradient magnitude of y in the i th pixel; $x_{i,j}$ denotes the distance between the i th pixel and its adjacent 8 pixels. The FAI gradient image is computed using Eq. (7) and given in Fig. 2b. As expected, high gradients occur around the boundaries of the algae slicks and within the algae slicks due to patchiness and the coarse resolution of MODIS (~250 m). This result suggests that the FAI gradient could be a better indicator than the FAI magnitude to differentiate algae slicks/patches from algae-free seawater. Indeed, FAI gradients have been utilized to statistically derive T_0 across entire MODIS scenes (Hu et al., 2010c; He et al., 2011; Zhang et al., 2014).

Most algae-free seawater pixels have small FAI gradients, except for the mud banks of the Subei Shoal or near the front between high SPM and lower SPM waters (Fig. 2b). These false positives need to be minimized. Because variation in the FAI of sediment-rich waters is mainly caused by variation in $R_{rc,645}$ (Fig. 2c), the latter may serve as a reference to correct the former:

$$cG_{FAI} = G_{FAI} - G_{R645} \quad (8)$$

where, G_{FAI} and G_{R645} denote gradients of FAI and $R_{rc,645}$, respectively. Fig. 2d shows the corrected FAI gradient image cG_{FAI} . Clearly, the high FAI gradients around the boundary of sediment patches are largely reduced, leading to a relatively homogeneous seawater background in the cG_{FAI} image, suggesting that a threshold of T_{cG} may be derived to delineate seawater pixels and algae-containing pixels in the cG_{FAI} image.

3.1.2. Determination of the threshold T_{cG}

All cloud-free MODIS images acquired between May and August were visually examined by linking the FAI image with the corresponding RGB image using the ENVI software to exclude images containing algae slicks. For each algae-free image, the corresponding cG_{FAI} image was derived using Eqs. (7)–(8). The histogram and cumulative histogram of all seawater pixels in each cG_{FAI} image were calculated, and the value corresponding to 0.99 in the cumulative histogram was selected as the T_{cG} for each image. The value 0.99 was chosen to exclude bright pixels due to small islands, fixed platforms, or ships.

3.1.3. Variable-window method

After applying the threshold T_{cG} to corrected FAI image, pixels were classified as algae-free seawater pixels ($\leq T_{cG}$) and candidate pixels ($> T_{cG}$), which may include algae-containing pixels and neighboring seawater pixels. To further classify the candidate pixels to seawater or algae-containing pixels, a variable-window method was implemented by varying window size to contain at least a certain number of seawater pixels to represent the local seawater background. The initial window size of this study was set to 11×11 , but the size was increased if the number of seawater pixels within the window was < 100 . For each

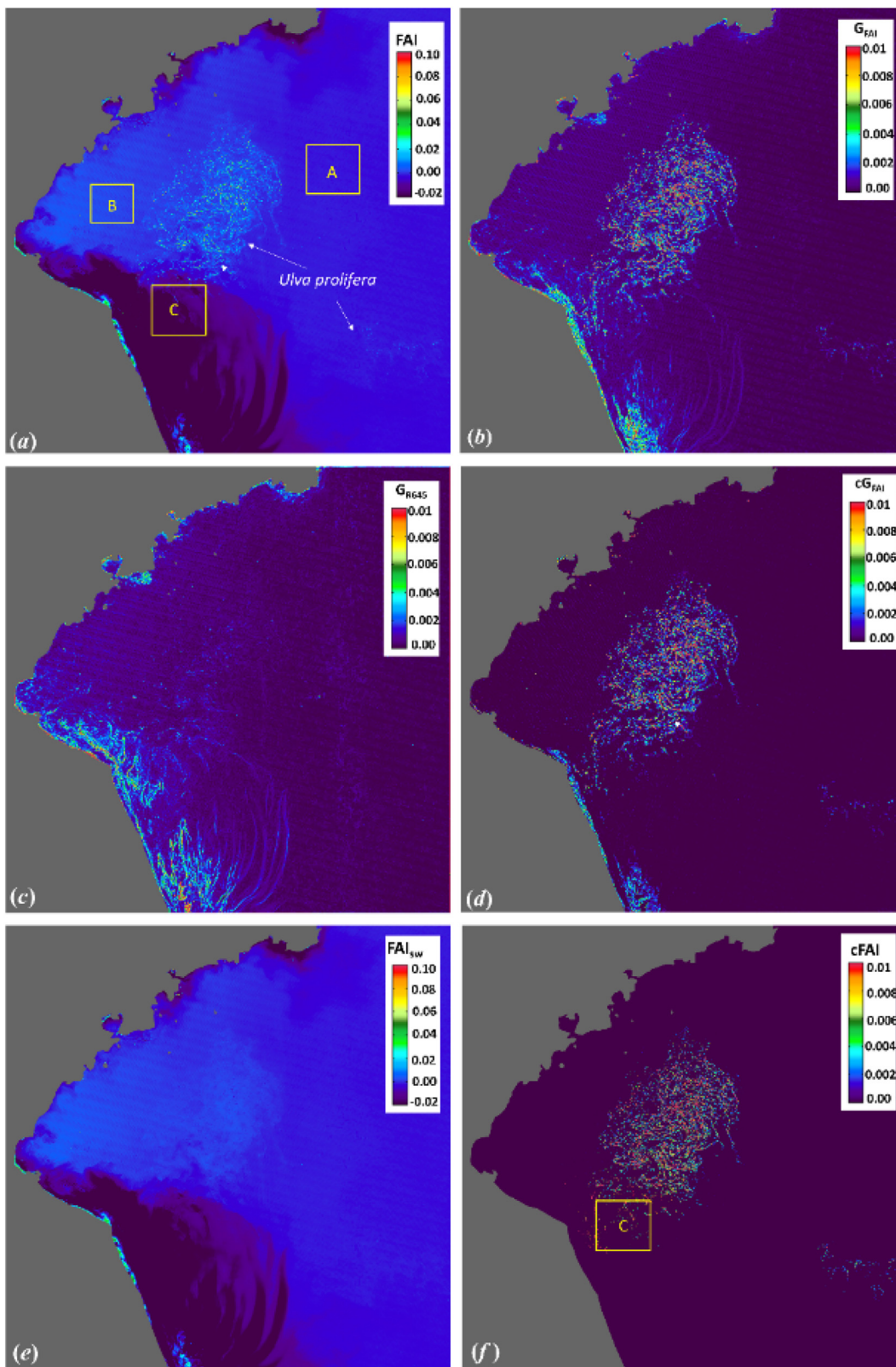


Fig. 2. (a) MODIS FAI image on 31 May 2008, with the corresponding RGB image shown in Fig. 1. Region A is a sunglint-free area, Region B is contaminated by sunglint (median $R_{rc,1240} = 0.085$), and Region C is located in the sediment plume area. (b) FAI gradient image G_{FAI} . (c) $R_{rc,645}$ gradient image G_{R645} . (d) Corrected FAI gradient image $cG_{FAI} = G_{FAI} - G_{R645}$. (e) Seawater background image, FAI_{sw} . (f) Corrected FAI image $cFAI = FAI - FAI_{sw}$.

candidate pixel, the mean ($FAI_{sw,mean}$) and standard deviation ($FAI_{sw,std}$) of seawater pixels within the kernel window were computed. The candidate pixel was classified as an algae-free seawater pixel if its

FAI value was $< FAI_{sw,mean} + 2 * FAI_{sw,std}$; otherwise, the pixel was classified as an algae-containing pixel. To construct the seawater background image FAI_{sw} , the FAI values of the classified algae-

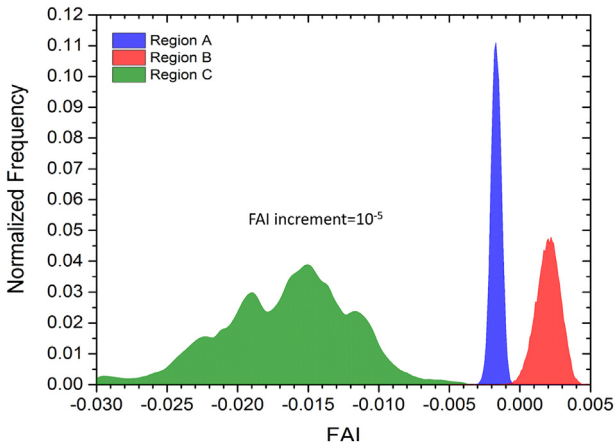


Fig. 3. Normalized histogram of FAI in Regions A, B, and C of Fig. 2a.

containing pixels were replaced by their corresponding $FAI_{sw,mean}$ values. The FAI_{sw} image corresponding to the above example is shown in Fig. 2e.

3.2. Determination of FAI_{algae}

The FAI of pure algae (FAI_{algae} , i.e., $\alpha = 1.0$ in Eqs. (4)–(6)) was taken as the upper bound to calculate α in the linear unmixing model of Eqs. (4)–(6). Both water tank and field experiments indicated that FAI linearly increased with algae biomass density (kg/m^2) for $FAI < 0.2$, but FAI appeared to plateau when algae biomass density exceeded 0.2

due to the vertical aggregation of algae (Hu et al., 2017). Thus, the inflection point ($FAI = 0.2$) in the FAI-biomass density curve can be regarded as FAI_{algae} . However, when applied to satellite images, atmospheric effects and sensor band settings need to be taken into account. In this study, radiative transfer simulations were used to estimate the perturbation of atmospheric FAI_{algae} (Hu, 2009):

$$R_{rc} = R_a + t_0 t R_{algae} \tag{9}$$

where R_a is the atmospheric reflectance due to aerosols and aerosol-Rayleigh interactions. R_{algae} is the pure-algae reflectance measured in the field with an FAI value of 0.2, t_0 is the atmospheric diffuse transmittance between the sun and sea surface, and t is the atmospheric transmittance from the *Ulva* to satellite sensor. Note that the value of t is actually between beam transmittance t_b and diffuse transmittance t_d depending on the algae distribution and bloom size. Generally, t is closer to t_b for small patches but closer to t_d for larger patches. Both t_b and t_d were used in this study to simulate FAI_{algae} .

The typical sun zenith angle (SZA) of the YS in the summer ($SZA = 18.4^\circ$) was used in the simulations. Two sensor viewing zenith angles were considered, with one ($VZA = 4^\circ$) for near-nadir viewing and the other ($VZA = 57^\circ$) for near side-side viewing. Two aerosol types (coastal aerosol with 50% humidity, C50, and maritime aerosol with 90% humidity, M90) and ten aerosol optical thicknesses at 859 nm varying from 0.03 to 0.4 (representing clear and turbid atmosphere) were considered in the simulations. For each scenario, R_a , t_0 and t_d were derived from the MODIS look-up tables of the SeaDAS software package, while t_b was computed from the aerosol optical thickness. After R_{rc} was simulated using Eq. (9), FAI_{algae} was calculated using Eq. (1) with the relative spectral response (RSR) function of MODIS. For application to other satellite sensors, the FAI_{algae} values for VIIRS/NPP,

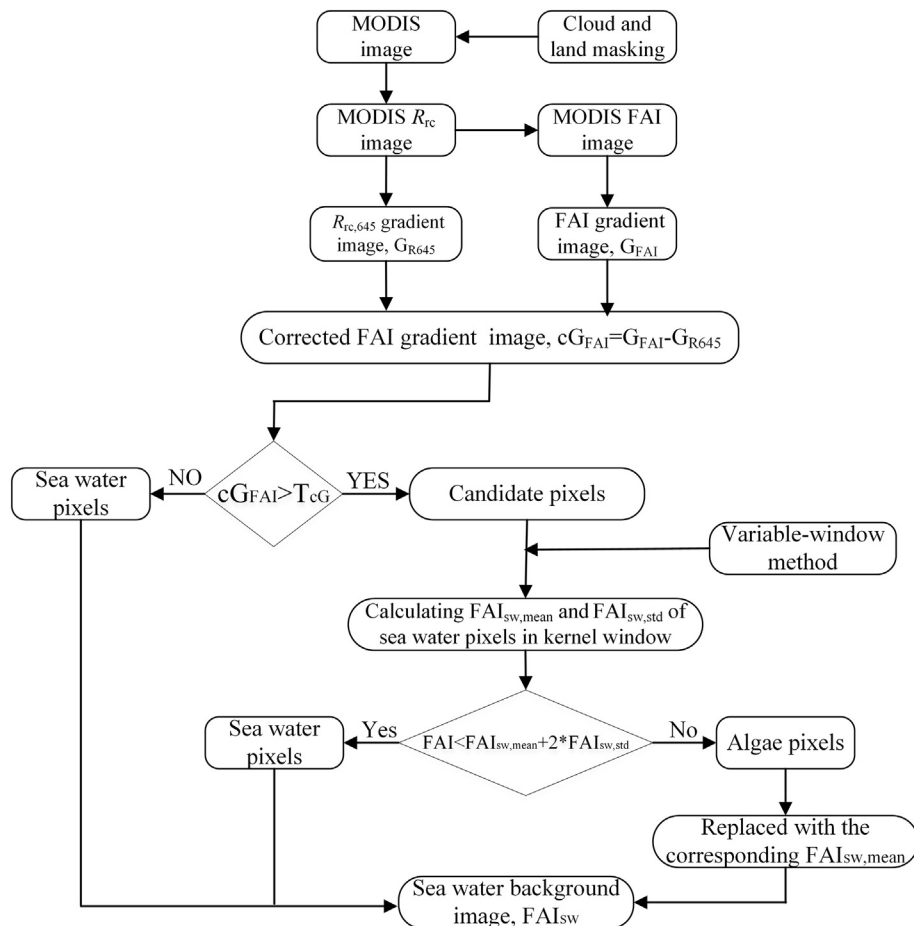


Fig. 4. Work flow to reconstruct the seawater background FAI image, FAI_{sw} .

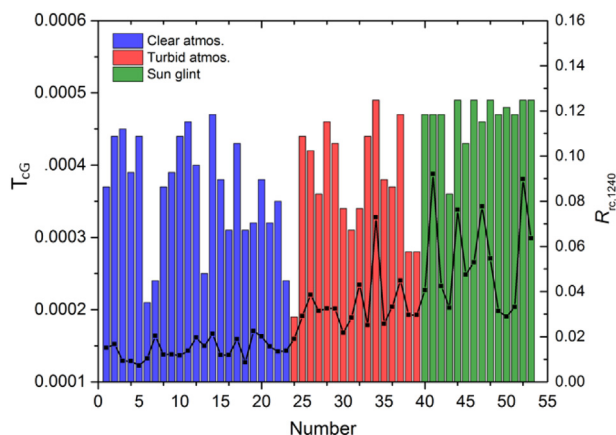


Fig. 5. Distributions of T_{CG} from 53 cloud-free and algae-free MODIS images. The blue, red and green colored areas represent MODIS images with clear atmosphere, turbid atmosphere, or sunglint contamination. The median $R_{rc,1240}$ values are also plotted (black curve) (y-axis to the right). The x-axis refers to the image number. (For interpretation of the references to color in this figure legend, the reader is referred to the web version of this article.)

OLCI/Sentinel-3, OLI/Landsat-8 and DVI_{algae} as an alternative index for satellite sensors in the absence of a SWIR band (e.g., WFV/GF-1 and WV-2) were computed using their specific RSR functions.

4. Results

4.1. Fixed threshold T_{CG}

Fig. 5 shows the histogram distribution of T_{CG} derived from 53 cloud-free and algae-free MODIS images between May and August from 2002 to 2016. The corresponding median $R_{rc,1240}$ values are also presented to indicate the turbidity of the atmosphere or the sunglint severity for each MODIS image. For clear-sky days, T_{CG} varies from 0.00015 to 0.0004, and $R_{rc,1240}$ is usually < 0.02 . For turbid atmosphere or sun glint days, T_{CG} varies from 0.00015 to 0.0005 and from 0.00025 to 0.00035, respectively, while $R_{rc,1240}$ is an average of 0.04 and 0.06 (up to 0.1), respectively. Under these three significantly different conditions, no clear pattern of T_{CG} can be found in Fig. 5. Therefore, the mean value of T_{CG} (0.00027) derived from 53 MODIS images was used as the fixed threshold to extract seawater pixels from the corrected FAI gradient image cG_{FAI} . A sensitivity test (Fig. 11) shows that the final estimation of algae coverage from individual MODIS images is insensitive to small changes in T_{CG} when this threshold is changed from 0.0002 to 0.0005.

4.2. FAI_{algae} and DVI_{algae} for different satellite sensors, with validation from WV-2

The simulated FAI_{algae} and DVI_{algae} for each sensor under different observing conditions (two viewing angles and three aerosol optical

thicknesses) are listed in Table 2. The numbers inside the parentheses are for simulations with atmospheric beam transmittance t_b , while the numbers outside the parentheses are for simulations with atmospheric diffuse transmittance t_d . For brevity, the simulation results for the two aerosol types are averaged. In addition to very clear ($\tau_{a,859} = 0.03$) and very turbid ($\tau_{a,859} = 0.4$) atmospheric conditions, Table 2 also presents the results corresponding to the typical aerosol loadings ($\tau_{a,859} = 0.16$) of the YS.

In general, FAI_{algae} and DVI_{algae} change slightly with VZA and aerosol optical thickness when atmospheric diffuse transmittance is used, reaching 15% for the worst case scenario (VZA = 57° and $\tau_{a,859} = 0.4$). However, if atmospheric beam transmittance is used, the changes can be half for the worst case scenario.

Because of the coarse resolution of MODIS data (~ 250 m), 99.5% algae-containing pixels have $\alpha < 1.0$ and are thus difficult to use to validate the simulated MODIS FAI_{algae} . Therefore, high-resolution WV-2 satellite data (2.0 m) were used to validate the simulated WV-2 DVI_{algae} . Fig. 6a shows the RGB image of WV-2, in which a number of algae patches can be clearly visualized. Among them, six large patches outlined by white boxes were extracted to show DVI distributions. The edge of each algae patch was excluded because the edge pixels may be mixed with algae and water (Fig. 6a inset). Other pixels within the patches were assumed to have a value of $\alpha = 1.0$. Fig. 6b shows the histogram and cumulative frequency distribution (CFD) of these algae pixels. The DVI of pure-algae pixels appears to have a normal distribution, varying from 0.16 to 0.31. When the CFD is 0.01 (99% pixels), the corresponding DVI value is 0.175 between the simulated DVI_{algae} values for WV-2 (0.167–0.192) for a nadir observation under the typical aerosol load of the YS. Such a close agreement confirms the simulated FAI_{algae} in this study.

4.3. Comparison of *Ulva* coverage derived from MODIS with high spatial resolution satellite OLI and WFV data

Generally, the derived *Ulva* areal coverages from MODIS data need to be validated with field measurements. However, it is nearly impossible to carry out such field experiments to concurrently measure the *Ulva* coverage corresponding to each 250-m MODIS pixel. Here, the *Ulva* areal coverages derived from MODIS are compared with two concurrent OLI/Landsat-8 scenes (30 m resolution) and ten WFV/GF-1 scenes (16 m resolution) as alternative ways of validation.

The overpassing times of OLI and WFV were both approximately 10:30 AM, close to the MODIS overpassing time. The method to estimate the *Ulva* areal coverage with OLI and WFV was the same as that used with MODIS (Section 3), but T_{CG} was statistically determined from the local seawater pixels in each image instead of using a fixed threshold. The FAI_{algae} or DVI_{algae} in typical aerosol loading at nadir viewing (bold font in Table 2) for the three sensors were used. The *Ulva* bloom areal coverage in the rectangular area derived from MODIS, MODISA and concurrent OLI/Landsat WFV/GF-1 are listed in Table 3. The numbers in the parentheses represent the relative percentage difference (RPD) values. The median VZA and $R_{rc,1240}$ values over the study regions are also listed in Table 3.

Table 2

FAI_{algae} and DVI_{algae} determined from simulations for each satellite sensor under different scenarios. The numbers inside the parentheses are for simulations with atmospheric beam transmittance t_b , while the numbers outside the parentheses are for simulations with atmospheric diffuse transmittance t_d .

Sensor	Index	λ (nm)	VZA = 4°			VZA = 57°		
			$\tau_{a,859} = 0.03$	$\tau_{a,859} = 0.16$	$\tau_{a,859} = 0.4$	$\tau_{a,859} = 0.03$	$\tau_{a,859} = 0.16$	$\tau_{a,859} = 0.4$
MODIS	FAI	645,859,1240	0.198 (0.192)	0.194 (0.167)	0.185 (0.127)	0.199 (0.185)	0.190 (0.146)	0.172 (0.089)
VIIRS	FAI	640,865,1610	0.191 (0.185)	0.187 (0.162)	0.179 (0.123)	0.193 (0.180)	0.184 (0.143)	0.167 (0.086)
OLCI	FAI	665,865,1020	0.162 (0.123)	0.158 (0.107)	0.151 (0.081)	0.162 (0.096)	0.154 (0.075)	0.140 (0.045)
OLI	FAI	665,865,1610	0.199 (0.193)	0.195 (0.169)	0.186 (0.128)	0.200 (0.187)	0.191 (0.147)	0.173 (0.090)
WFV/GF-1 WV-2	DVI	660,830	0.197 (0.192)	0.192 (0.167)	0.181 (0.125)	0.198 (0.186)	0.187 (0.145)	0.166 (0.085)

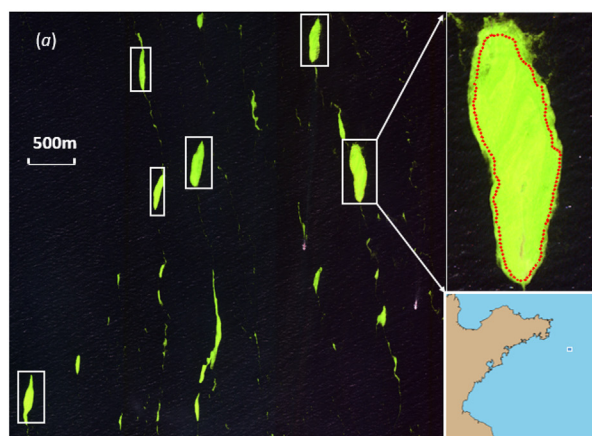


Fig. 6. (a) WorldView-2 RGB sub-image acquired on 23 June 2012 over the YS centered at 36.650°N, 122.741°E. The six large algae patches outlined in the white boxes are selected to derive the DVI distributions. The pixels at the edge of each patch may be mixed with seawater and are therefore excluded in subsequent calculation. (b) Histogram and cumulative frequency distribution (CFD) of DVI in the polygon area of six large patches in the WV-2 image. When CFD = 0.01, the corresponding DVI = 0.175, indicating that 99% of the pixels in the polygon areas have DVI values > 0.175.

Generally, the *Ulva* coverage derived from MODIS agrees well with those derived from higher-resolution data. The mean RPD is 9.6%, and the maximum RPD is 21%. Underestimation usually occurs at high VZA values, which can be attributed to the following reasons. First, FAI_{algae} and DVI_{algae} both decrease with increasing VZA, varying from 2% to 13% depending on whether diffuse or beam atmospheric transmittance is considered (Table 2). Therefore, the use of FAI_{algae} and DVI_{algae} at nadir view underestimates the *Ulva* areal coverage for pixels with large VZAs (see Eq. (6)). Second, the MODIS pixel size at high VZA (e.g., 60°) is 3–4 times larger than at nadir (Wolfe et al., 1998); thus, small algae patches are possibly missed. Finally, serious “bowtie” effects occur at MODIS image edges due to the overlap of consecutive scan lines, leading to degraded data quality (Tan et al., 2006).

In Table 3, four MODIS scenes are contaminated by sunglint (marked * after $R_{rc,1240}$ in Table 3) with median $R_{rc,1240}$ values varying from 0.060 to 0.164; these values are much higher than the average $R_{rc,1240}$ of ~0.02 in cloud-free and glint-free days. The *Ulva* areal coverage derived from sunglint-contaminated MODIS images agrees well with that derived from the concurrent glint-free WFV/GF-1 images

(RPD ~9.2%), suggesting that the method developed in this study is tolerant to sunglint contamination.

4.4. *Ulva* areal coverage and biomass between 2008 and 2016 in the YS

In such estimates, the fixed $T_{CG} = 0.00027$ was used for all MODIS data to reconstruct the seawater background image (FAI_{sw}), and FAI_{algae} values corresponding to typical aerosol loadings ($\tau_{a, 859} = 0.16$) for atmospheric diffuse and beam transmittances, as shown in Table 2, were selected and interpolated according to the actual VZA over the *Ulva* patches. The means and standard deviations of the estimated *Ulva* areal coverage are given in Table 4, where bold numbers represent the maximums for each year. The *Ulva* areal coverage on 30 May of 2008 is 220 km², significantly lower (1.1–16 times) than values in earlier reports (Table 1). Qi et al. (2016) estimated the maximum coverage in daily observation between 2007 and 2015 by using manually adjusted T_0 values. The results reported for 2008, 2014, and 2015 agree well with those from this study. Their unpublished result for 30 May 2008, 234 km² (Table 1), is also consistent with this study. However, the

Table 3

Ulva areal coverage estimated from MODIS/Terra (MODIST), MODIS/Aqua (MODISA), concurrent high-resolution OLI/Landsat and WFV/GF-1. The numbers in the parentheses are the relative percent difference (RPD) values from the high-resolution estimate. For reference, the VZA, median $R_{rc,1240}$ of MODIS, and threshold T_{CG} used for high-resolution data are also listed.

Date	Region	<i>Ulva</i> coverage (km ²)			T_{CG}	VZA		$R_{rc,1240}$	
		OLI	MODIST	MODISA		MODIST	MODISA	MODIST	MODISA
2016-06-25	35.357°–35.935°N, 120.561°–121.437°E	225	201 (10.6)	247 (9.6)	0.0004	62	12	0.022	0.026
	35.215°–36.612°N, 121.425°–122.170°E	262	227 (13.4)	298 (13.4)	0.0004	64	19	0.021	0.020
	34.525°–35.450°N, 120.378°–121.453°E	267	213 (12.3)	259 (2.9)	0.0004	63	11	0.017	0.020
Date	Region	WFV	MODIST	MODISA	WFV	MODIST	MODISA	MODIST	MODISA
2013-06-13	34.735°–35.043°N, 120.487°–120.987°E	86	86 (0.7)	85 (1.0)	0.0004	45	48	0.019	0.018
2014-06-18	35.426°–35.652°N, 120.015°–120.588°E	14	13 (6.2)	15 (9.6)	0.0004	58	29	0.017	0.013
2014-06-18	34.518°–35.242°N, 120.483°–121.385°E	192	215 (12.0)	214 (11.6)	0.0004	56	32	0.017	0.015
2015-05-24	34.141°–34.486°N, 121.042°–121.555°E	71	62 (12.4)	–	0.0004	55	–	0.010	–
2015-06-06	35.003°–35.668°N, 120.865°–122.156°E	136	133 (2.0)	–	0.0004	14	–	0.096 ^a	–
2015-06-27	36.539°–36.793°N, 121.686°–122.291°E	42	50 (19.1)	46 (9.9)	0.0004	42	24	0.014	0.043
2015-06-27	34.879°–35.342°N, 120.648°–121.091°E	35	39 (10.9)	–	0.0008	40	–	0.016	–
2015-07-04	35.619°–36.339°N, 120.927°–122.155°E	250	293 (17.0)	301 (20.5)	0.0003	49	18	0.014	0.164 ^a
2015-07-08	36.328°–36.669°N, 121.285°–121.774°E	72	71 (2.1)	74 (2.9)	0.0004	11	51	0.137 ^a	0.015
2016-06-01	34.490°–35.138°N, 121.074°–121.464°E	85	95 (11.7)	78 (8.5)	0.0004	1	59	0.060 ^a	0.031

– MODIS data are covered by cloud.

^a MODIS data are contaminated by sunglint.

Table 4

Ulva areal coverage estimated from cloud-free MODIS data between 2008 and 2016. Numbers in bold font represent the daily maximum in that year.

Year	<i>Ulva</i> areal coverage (km ²)						
2008	May 20	May 30	May 31	June 25	June 29		
	26 ± 2	220 ± 31	257 ± 35	455 ± 60	228 ± 27		
2009	June 22	June 24	July 1	July 2	July 15		
	134 ± 9	230 ± 17	203 ± 17	281 ± 20	196 ± 23		
2010	June 5	June 7	June 21	June 28	July 6	July 11	
	12 ± 1	14 ± 1	92 ± 12	49 ± 6	152 ± 20	32 ± 2	
2011	May 28	June 1	June 13	June 19	July 11		
	5 ± 0	26 ± 2	121 ± 8	165 ± 20	22 ± 3		
2012	May 26	May 28	June 12	July 06			
	47 ± 6	57 ± 7	86 ± 10	36 ± 4			
2013	June 2	June 13	June 20	June 29	July 24		
	130 ± 9	381 ± 49	637 ± 75	430 ± 55	17 ± 2		
2014	May 23	May 26	May 28	June 18	July 3	July 11	
	87 ± 12	168 ± 20	124 ± 9	533 ± 61	397 ± 52	342 ± 44	
2015	May 20	May 25	June 5	June 12	June 21	July 1	July 4
	94 ± 10	375 ± 49	597 ± 69	875 ± 119	1153 ± 156	725 ± 48	716 ± 90
2016	May 17	May 25	June 1	June 16	June 25	July 21	
	38 ± 2	254 ± 16	398 ± 28	1252 ± 138	1350 ± 90	22 ± 2	

method developed here can be implemented for operational monitoring without manual intervention.

An example of an extensive *Ulva* bloom and its evolution in 2015 is shown in Fig. 7. *Ulva* coverage started to increase in approximately

mid-May in the Subei Shoal and moved northward following winds and currents. By mid-June, the bloom peaked and approached Qingdao, and then dissipated in early July and disappeared between the end of July and early August. Some new *Ulva* slicks appeared in the Subei Shoal at

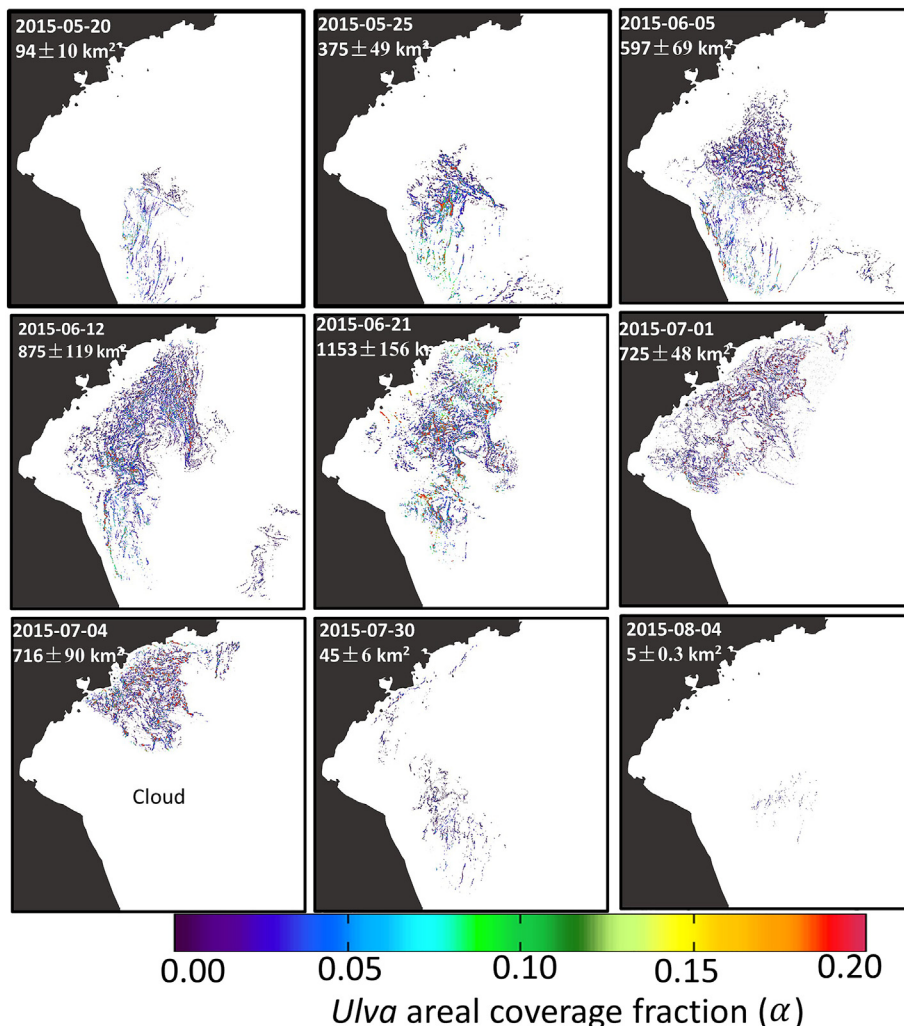


Fig. 7. *Ulva* coverage fraction (α) and evolution for the 2015 bloom event, derived from MODIS data. Estimates of total *Ulva* areal coverage are annotated on each image. $\alpha = 0.10$ means 10% of the pixel is covered by *Ulva*.

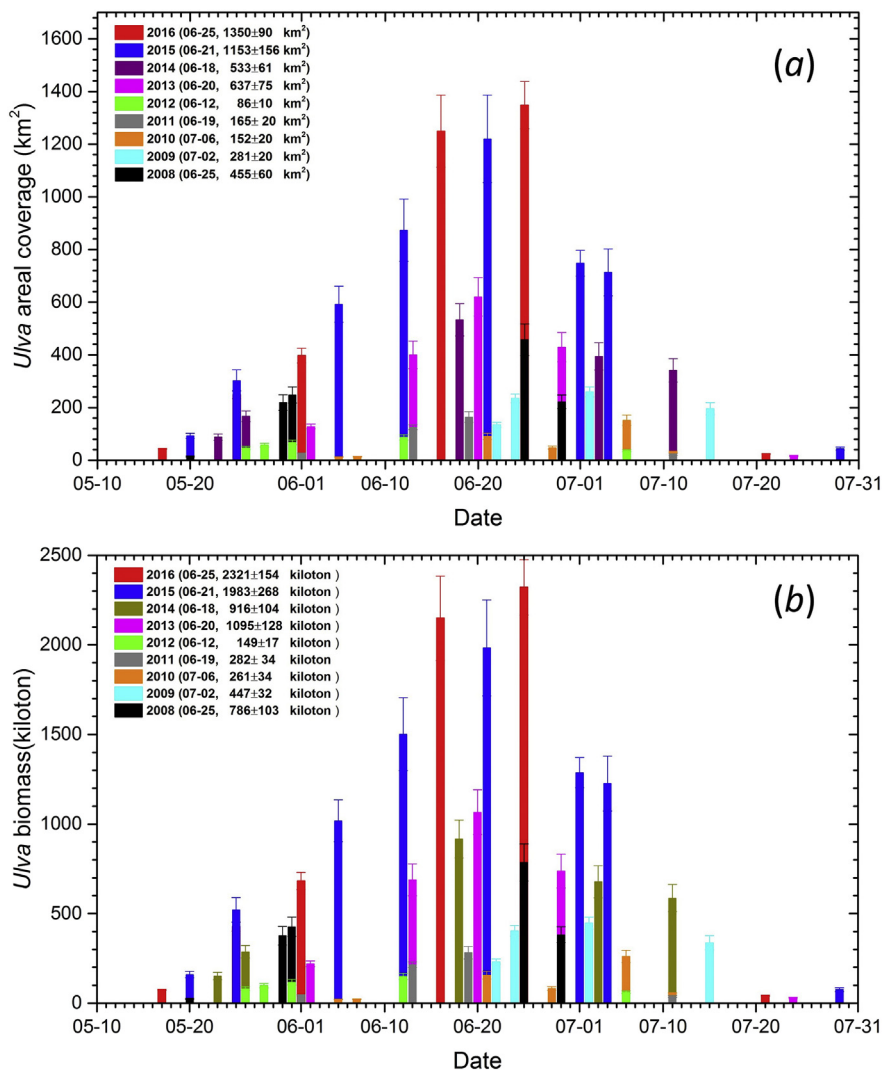


Fig. 8. (a). Daily *Ulva* areal coverage in the YS derived from near cloud-free and sunglint-free MODIS data between 2008 and 2016 using both diffuse and direct atmospheric transmittance. The error bars represent standard deviations. The maximum daily coverage are listed in parentheses for each year. (b) same as (a) but for *Ulva* total biomass.

the end of July but quickly declined. The *Ulva* areal coverage on 21 June 2015 reached a maximum of 1153 km².

The daily change rate of *Ulva* areal coverage is defined as:

$$S_{tn} = S_{t0} * (1 + d)^n \tag{10}$$

where S_{t0} is the *Ulva* areal coverage at day 0, S_{tn} is the coverage at day n, and d is the daily change rate. During the early bloom stage between 20 May and 25 May, *Ulva* rapidly aggregated with an increasing rate up to 34% day⁻¹. Then, the increasing rate gradually decreased and stabilized to ~5–7% day⁻¹ between 25 May and 21 June. In an in situ enclosure experiment, Zhang et al. (2013) also found that *Ulva* rapidly grew in the early accelerated phase (up to 58% day⁻¹) and then remained relatively stable at a lower growth rate.

The *Ulva* coverage time series derived from MODIS is shown in Fig. 8a. Because both *Ulva* areal coverage and biomass increase linearly with FAI (Hu et al., 2017), *Ulva* total biomass can be derived from *Ulva* areal coverage, as shown in Fig. 8b. Although the time series is not continuous in time due to frequent cloud cover, the seasonal patterns and inter-annual changes in the *Ulva* areal coverage and total biomass can still be clearly visualized. In 2016, the maximum daily coverage reached 1350 km². Between 2010 and 2012, the maximum daily coverage was < 165 km². Several studies have attempted to explain the causes of inter-annual bloom variability. Lee et al. (2011) attributed the

massive *Ulva* bloom in 2008 to upwelling in the bloom transport pathway; however, Keesing et al. (2011) found no change in water temperature and wind patterns for the bloom years of 2008 and 2009. More recently, Qi et al. (2016) examined potential factors that could affect the bloom size, including seaweed aquaculture area, water pollution, sea surface temperature (SST), photosynthetically active radiation (PAR), precipitation, and wind anomalies over the YS between 2007 and 2015. However, no conclusion could be drawn to explain the reasons underlying the high inter-annual bloom variability.

5. Discussion

5.1. Which index should be used?

As shown in Table 1, most publications on *Ulva* remote sensing have used NDVI to detect *Ulva* and quantify *Ulva* coverage. Although simple to implement and apply, NDVI is sensitive to atmospheric conditions (e.g., variable aerosols, sunglint, and thin clouds) and sun/sensor viewing geometry (Hu, 2009). This may not be a problem for the image visualization or image segmentation of a small region. However, for large regions or different days, different image stretch settings may be required for visualization. Most importantly, the nonlinear design makes it difficult to unmix a pixel. Fig. 9a shows the scatter plot

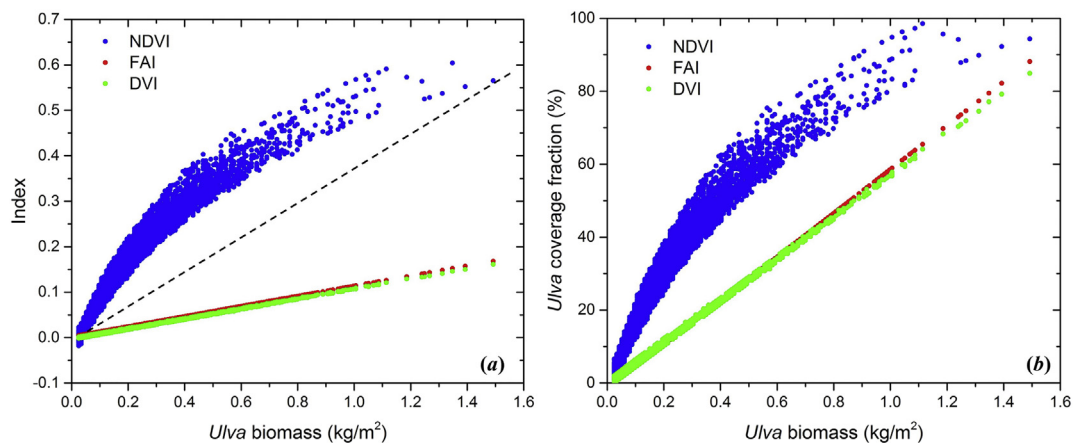


Fig. 9. (a) Scatter plot of FAI, NDVI, and DVI versus *Ulva* biomass density for all algae-containing pixels on 31 May 2008 (Fig. 2a). The dashed black line indicates the linear unmixing model used for NDVI when estimating *Ulva* areal coverage. (b) Scatter plot of the calculated *Ulva* coverage fraction versus *Ulva* biomass density.

between the various indexes (FAI, NDVI, and DVI) and *Ulva* biomass density for all algae-containing pixels on 31 May 2008, for which the *Ulva* biomass density of each algae-containing pixel was calculated using a remote *Ulva* biomass model (Hu et al., 2017). The figure clearly shows that NDVI is nonlinear to *Ulva* biomass density, which is nearly saturated at 1.6 kg/m². In contrast, both FAI and DVI show a linear relationship with biomass density. This suggests that *Ulva* coverage calculated from NDVI using a linear unmixing model can be overestimated significantly (Fig. 9b), while FAI and DVI do not suffer from this problem. In the absence of a SWIR band, DVI may be a good alternative to FAI; otherwise, FAI should be used because as long as aerosol reflectance is spectrally linear, FAI is completely immune to aerosol changes. The requirement of DVI on aerosol reflectance is more conservative because there are only two bands used to account for aerosol perturbations.

5.2. Resolution versus areal coverage

Compared with high-resolution (1–2 m) sensors, coarse-resolution sensors may either underestimate or overestimate *Ulva* coverage for two contrasting reasons. The first reason is easy to understand: high-resolution sensors can capture more small algae patches than coarse-resolution sensors, leading to underestimates by the latter (Hu et al., 2015; Hu et al., 2016a). Hu et al. (2015) simulated and analyzed the spectral and spatial requirements for the detection of floating macroalgae by satellite sensors. The results show that for SNRs of 200:1, the minimum spatial coverage of the macroalgae that can be detected is approximately 1–2% of a pixel, suggesting that small *Ulva* patches (< 1–2% of the MODIS pixel size) will be missed in MODIS 250 m resolution data.

On the other hand, the second explanation for why coarse-resolution sensors may overestimate *Ulva* coverage even after pixel unmixing is counterintuitive. This overestimation can be the result of the averaging effect that occurs when *Ulva* aggregate to form small yet very thick patches, with FAI values reaching > 0.2 (Hu et al., 2010c; Hu et al., 2017). These high values of *Ulva* indexes (e.g., FAI, NDVI and DVI) from small, thick patches within a pixel are unmixed using a T_1 threshold lower than 0.2, leading to an overestimation after unmixing. Indeed, such an overestimation by coarse-resolution sensors has been reported earlier (Cui et al., 2012; Zhang et al., 2014; Xu et al., 2016).

The two contrasting processes can be illustrated in the simulation study below. In the simulation, high-resolution WV-2 (2 m) data were used to simulate medium-resolution (30 m, OLI) and coarse-resolution (250 m, MODIS) data. Fig. 10 shows the DVI images of the original 2 m WV-2 data and simulated 30 m and 250 m data. Many of the small patches in the 2 m data cannot be found in the 30 m and 250 m data,

illustrating the first process. On the other hand, the high-DVI patches (DVI > T_1) in the WV-2 image are smeared in the lower-resolution images, illustrating the second process. Using $DVI_{\text{algae}} = 0.192$ (Table 2) and $DVI_{\text{sw}} = -0.015$ (derived from WV-2 seawater pixels), the *Ulva* area coverages estimated from Eq. (3) are 0.407, 0.400, and 0.457 km² for the 2, 30, and 250 m data, respectively. The 12.3% increase in the 250 m data compared to the original 2 m resolution data indicates that process 2 overwhelms process 1. This is because there are 54,860 pixels with DVI > 0.192 in the original 2-m resolution data, and all these pixels are averaged with neighboring pixels with lower DVI values (e.g., seawater pixels) when simulating the coarse-resolution data.

However, this single case should not be generalized. During early stages of *Ulva* blooms, the bloom patches may be very small and thus may be underestimated by coarse-resolution sensors. During peak blooms, the patches may be much larger, leading to overestimates in the bloom coverage for the reasons outlined above.

5.3. Viewing angle, atmospheric conditions, and *Ulva* areal coverage

Both the VZA and atmospheric conditions may impact the estimated *Ulva* areal coverage. Seventeen cloud-free MODIST and MODISA same-day image pairs (~2 h apart) were used to understand such impacts, where the two thresholds were used as $FAI_{\text{algae}} = 0.194$ and $T_{\text{CG}} = 0.00027$. Table 5 lists the estimated *Ulva* coverage and relative percent difference (RPD) between MODIST and MODISA, as well as their corresponding VZA, $R_{\text{rc},1240}$, and atmospheric conditions. The 17 image pairs were partitioned into four Groups. In Group 1, MODIST and MODISA had a clear atmosphere but different VZA values. In Group 2, MODIST and MODISA had contrasting atmospheres (clear or turbid) and VZA values. In Group-3, MODIST and MODISA had similar turbid atmosphere or glint conditions. In Group 4, MODIST and MODISA had either a sun glint or turbid atmosphere. Table 5 suggests that (1) for similar VZA and atmospheric conditions, the *Ulva* areal coverages derived from MODIST and MODISA agree very well (e.g., < 3.5% RPD for the first three MODIS pairs in Group 1); (2) under similar atmospheric conditions, a high VZA tends to underestimate the *Ulva* areal coverage (e.g., 27.7% underestimates for the 2 June 2013 case in Group 1); (3) under turbid atmosphere and sun glint conditions, *Ulva* areal coverage tends to be underestimated (up to 45%). Clearly, to derive accurate coverage (and therefore biomass) information, the uncertainties caused by these factors should be considered.

5.4. Uncertainties in the estimation of *Ulva* areal coverage

Because of the linear mixing of *Ulva* and seawater in affecting the

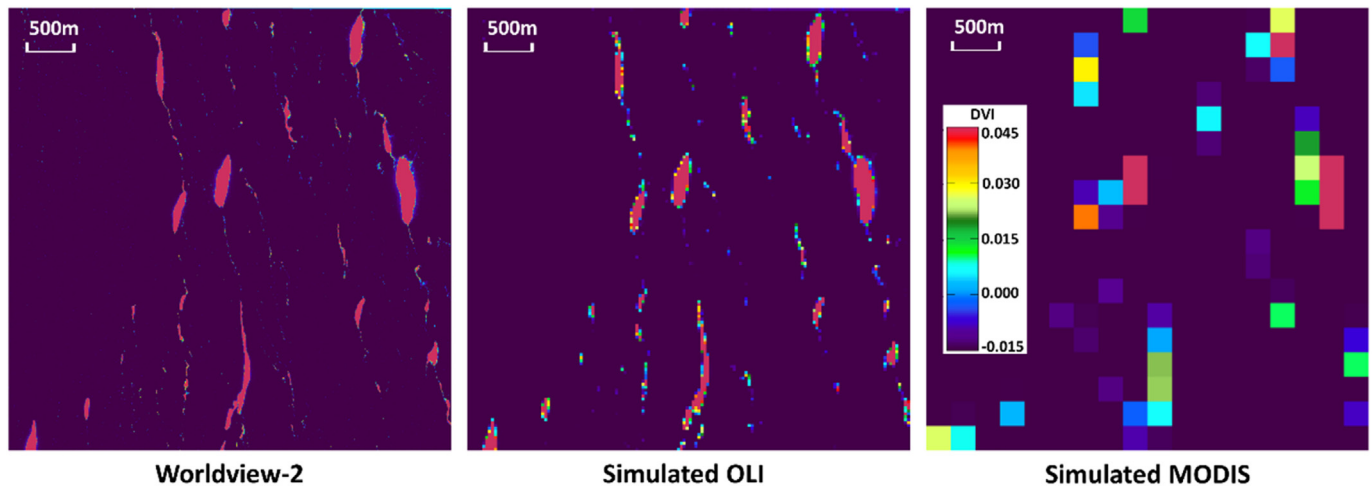


Fig. 10. Comparison between DVI image of high-resolution (2 m) WV-2 data, simulated medium-resolution (30 m) data and coarse-resolution (250 m) data. The image size of simulated OLI and MODIS are enlarged to the same size with WV-2 (2250 * 2250).

reflectance (therefore FAI), uncertainties in the estimation of *Ulva* coverage mainly comes from the selection of the lower- and upper-bound thresholds. In this study, instead of using a global threshold T_0 for the lower bound, a reconstructed seawater background image (FAI_{sw}) was used to minimize the impact of variable atmospheric and oceanic properties on the threshold, and the upper bound (100% coverage within a pixel) was carefully determined from field experiments and simulated for various sensor and atmosphere settings. However, these uncertainties cannot be eliminated for the following reasons.

The seawater background appears to have some spatial features

associated with *Ulva* algae patches as shown in Fig. 2e. The reason is that those seawater pixels are contaminated by the surrounding *Ulva* pixels (adjacent effects) resulting in slightly higher FAI values than seawater pixels further away from the algae pixels. This phenomenon usually occurs in extensive *Ulva* patches where most seawater pixels in the variable-window are from algae-adjacent pixels. Increasing the initial window size and using a larger number of seawater pixels to calculate histograms could somehow reduce this effect, yet a larger number of seawater pixels may not well represent the local background. A sensitivity test using a much larger window size showed that

Table 5

Ulva areal coverage derived from 17 MODIST and MODISA image pairs and their relative percent difference (RPD), VZA, $R_{rc,1240}$, and atmospheric conditions for each image are also given.

Groups	Date	Sensor	Coverage (km ²) and RPD (%)	VZA (°)	$R_{rc,1240}$	Atmos. Cond.	
Group-1	2010-06-21	MODIST	80	-1.9	47	0.008	Clear
		MODISA	78		45	0.009	Clear
	2013-06-29	MODIST	362	-3.3	45	0.012	Clear
		MODISA	375		48	0.013	Clear
	2013-06-20	MODIST	552	-3.1	34	0.013	Clear
		MODISA	535		53	0.013	Clear
	2015-05-25	MODIST	360	-6.6	29	0.006	Clear
		MODISA	336		57	0.009	Clear
	2013-06-02	MODIST	121	-27.7	16	0.019	Clear
		MODISA	87		63	0.015	Clear
2016-06-25	MODIST	1051	-16.5	63	0.02	Clear	
	MODISA	1260		16	0.02	Clear	
Group-2	2009-07-15	MODIST	104	-40.1	59	0.016	Turbid Atmos.
		MODISA	173		29	0.011	Clear
2014-05-26	MODIST	92	-37.4	60	0.022	Turbid Atmos.	
	MODISA	148		22	0.016	Clear	
Group-3	2014-06-18	MODIST	414	-12.3	56	0.025	Turbid Atmos.
		MODISA	472		33	0.016	Turbid Atmos.
2008-05-31	MODIST	219	-1.2	35	0.049	Sunglint	
	MODISA	222		40	0.036	Sunglint	
2014-05-27	MODIST	80	-30.3	3	0.056	Turbid Atmos.	
	MODISA	56		59	0.047	Turbid Atmos.	
Group-4	2008-05-20	MODIST	14	-44.3	54	0.041	Turbid Atmos.
		MODISA	25		12	0.102	Sunglint
2009-07-01	MODIST	106	-43.6	60	0.025	Turbid Atmos.	
	MODISA	188		7	0.047	Sunglint	
2014-05-28	MODIST	82	-28.9	59	0.018	Turbid Atmos.	
	MODISA	116		3	0.046	Sunglint	
2015-07-01	MODIST	677	-4.5	4	0.056	Sunglint	
	MODISA	647		58	0.028	Turbid Atmos.	
2016-06-01	MODIST	370	-10.8	4	0.073	Sunglint	
	MODISA	330		58	0.030	Turbid Atmos.	
2016-06-17	MODIST	797	-10.4	6	0.085	Sunglint	
	MODISA	714		58	0.025	Turbid Atmos.	

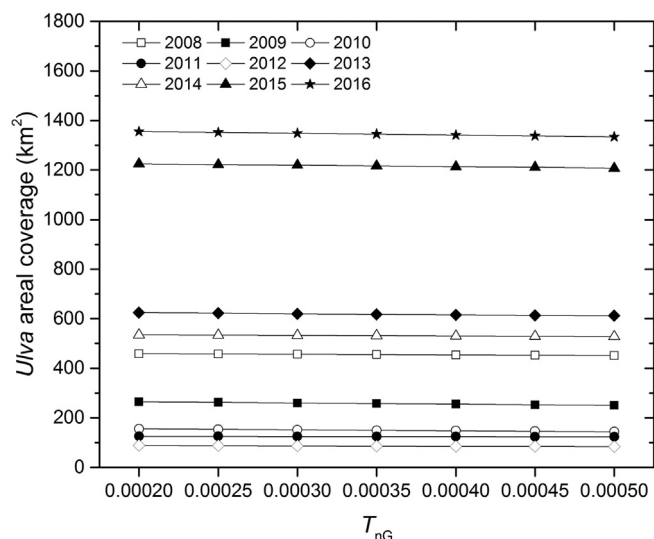


Fig. 11. Sensitivity of the *Ulva* areal coverage estimates from individual MODIS images to the selection of the threshold T_{nG} .

increased algae coverage by $\sim 4\%$, indicating that the algae coverage in this study might be slightly underestimated.

The threshold T_{nG} was derived from 53 cloud-free and algae-free MODIS images between May and August from 2002 to 2016, which varied from 0.0002 to 0.0005. The sensitivity of the final estimated *Ulva* areal coverage to changes in T_{nG} is shown in Fig. 11, where the estimation was made for the maximum daily images in 2008–2016. It is clear that for the entire range of T_{nG} , the estimated algae coverage only changed by a few percent (e.g., 1.5% for the 2016 image).

The upper-bound threshold, corresponding to 100% algae coverage within a pixel (i.e., FAI_{algae}), was determined from water tank and in situ experiments, and propagated to top of atmosphere to include typical aerosol effects. Sensitivity analysis showed that using a fixed FAI_{algae} for typical conditions may result in $\sim 6.5\text{--}12\%$ uncertainties under variable aerosol conditions (Hu et al., 2017). Considering all these factors together, the overall uncertainties in the *Ulva* coverage estimates are estimated to be $\sim 20\%$ or less.

Another uncertainty source may come from the bidirectional reflectance of *Ulva* (BRDF effect), which is unfortunately difficult to quantify as its measurement is simply not available. Considering the consistency between the water tank experiment and in situ experiment when their viewing angle changed from $\sim 0^\circ$ (i.e., vertical view) to $\sim 45^\circ$ (side view), the uncertainties in the satellite-based estimates due to the BRDF effects may be small for view angles $< 45^\circ$. This is actually confirmed by the comparison between same-day MODIST and MODISA measurements (Table 5) and by the agreement between simulated DVI_{algae} with observed DVI_{algae} from the high-resolution WV-2 measurement with a 20° viewing angle.

FAI_{algae} may change between *Ulva* growing and decaying stages as they may contain different concentrations of chlorophyll, which may change the color appearance (therefor FAI) of macroalgae (Vahtmäe et al., 2018; Thorhaug et al., 2007) or land vegetation (Boyer et al., 1988; Carter and Spiering, 2002). Future studies need to quantify such changes from both field and satellite measurements. Likewise, the impacts of *Ulva* at depth (as opposed to floating on the surface) due to either hydrodynamics (Lü and Qiao, 2008) or *Ulva* decay need to be quantified.

Finally, like any other studies to estimate macroalgae coverage, there is no in situ validation due to reasons outlined earlier (Wang and Hu, 2016; Hu et al., 2017). Briefly, this is because that it is nearly impossible to sample the entire water area corresponding to one or more satellite pixels at the same time. However, because high-resolution (~ 2.0 m) WV-2 measurements can capture many of the small *Ulva*

patches with full pixel coverage, WV-2 data used in this study essentially serve as ground truth to validate the coarse-resolution MODIS estimates.

6. Conclusions

Since 2008, several methods have been developed to identify *Ulva* blooms and quantify their areal coverage in the YS, with results often demonstrating > 10 -fold differences due to different choices in distinguishing algae-containing pixels from algae-free pixels and/or in unmixing coarse-resolution pixels. The novelty of this study is that, an objective method is developed to address this technical challenge, in which a corrected gradient image (cG_{FAI}) is used to identify algae-containing pixels, and a seawater background image is reconstructed to provide local threshold values (T_0) to represent 0% algae coverage. While the upper bound for 100% *Ulva* coverage is carefully determined from field experiments with sensor and atmosphere settings, the cG_{FAI} approach largely reduces the impacts of suspended sediments, atmospheric turbidity, and sunglint on the final coverage estimates. Consequently, an objective method is developed to eliminate the need for manual intervention to account for those variable conditions, leading to accurate estimations of *Ulva* areal coverage and biomass (as validated by high-resolution imagery). However, extreme observing conditions such as large viewing angles or high atmospheric turbidity may still lead to relatively high uncertainties, which should be considered when estimating bloom size or studying bloom trends.

Acknowledgements

This work was supported by the National Natural Science Foundation of China (Nos. 61675187 and 60638020), Qingdao Science and Technology Project (No. 14-9-3-2-HY), and Dragon 4 Programme (project ID 32281). We thank the NASA MODIS team for providing MODIS data, USGS for providing Landsat data, and CRESDA for providing GF-1 data. We are grateful for three anonymous reviewers for their valuable comments and suggestions to improve this manuscript.

References

- Boyer, M., Miller, J., Belanger, M., Hare, E., Wu, J., 1988. Senescence and spectral reflectance in leaves of northern pin oak (*Quercus palustris* Muenchh.). *Remote Sens. Environ.* 25, 71–87. [https://doi.org/10.1016/0034-4257\(88\)90042-9](https://doi.org/10.1016/0034-4257(88)90042-9).
- Carter, G.A., Spiering, B.A., 2002. Optical properties of intact leaves for estimating chlorophyll concentration. This project was supported by a grant from the Office of Technology Transfer, NASA, Stennis Space Center. *J. Environ. Qual.* 31, 1424–1432. <https://doi.org/10.2134/jeq2002.1424>.
- China SOA, 2016. Bulletin of marine environmental status of China. <http://www.soa.gov.cn/zwgf/hygf/zghyhjzlgf/>.
- Cui, T., Zhang, J., Sun, L., Jia, Y., Zhao, W., Wang, Z., Meng, J., 2012. Satellite monitoring of massive green macroalgae bloom (GMB): imaging ability comparison of multi-source data and drifting velocity estimation. *Int. J. Remote Sens.* 33, 5513–5527. <https://doi.org/10.1080/01431161.2012.663112>.
- Ding, Y., Cao, C., Huang, J., Zhong, S., Wang, N., Hu, W., Gao, S., 2015. The green tide multi-source satellite remote sensing operational monitoring requirement analysis and system design in the Yellow Sea (in Chinese with English abstract). *Mar. Sci.* 39, 85–90.
- Duan, H., Loiselle, S.A., Zhu, L., Feng, L., Zhang, Y., Ma, R., 2015. Distribution and incidence of algal blooms in Lake Taihu. *Aquat. Sci.* 77, 9–16. <https://doi.org/10.1007/s00027-014-0367-2>.
- Feng, L., Li, J., Gong, W., Zhao, X., Chen, X., Pang, X., 2016. Radiometric cross-calibration of Gaofen-1 WFV cameras using Landsat-8 OLI images: a solution for large view angle associated problems. *Remote Sens. Environ.* 174, 56–68. <https://doi.org/10.1016/j.rse.2015.11.031>.
- Garcia, R.A., Fearn, P., Keesing, J.K., Liu, D., 2013. Quantification of floating macroalgae blooms using the scaled algae index. *J. Geophys. Res. Oceans* 118, 26–42. <https://doi.org/10.1029/2012JC008292>.
- He, M.-X., Liu, J., Yu, F., Li, D., Hu, C., 2011. Monitoring green tides in Chinese marginal seas. In: Jesus Morales, V.S., Platt, Trevor, Sathyendranath, Shubha (Eds.), *Handbook of Satellite Remote Sensing Image Interpretation: Applications for Marine Living Resources Conservation and Management*. EU PRESPO and IOCCG, Dartmouth, Canada, pp. 111–124.
- Hu, C., 2009. A novel ocean color index to detect floating algae in the global oceans. *Remote Sens. Environ.* 113, 2118–2129.
- Hu, C., He, M.-X., 2008. Origin and offshore extent of floating algae in Olympic sailing

- area. EOS Trans. Am. Geophys. Union 89, 302–303. <https://doi.org/10.1029/2008eo330002>.
- Hu, C., Cannizzaro, J., Carder, K.L., Muller-Karger, F.E., Hardy, R., 2010a. Remote detection of *Trichodesmium* blooms in optically complex coastal waters: examples with MODIS full-spectral data. Remote Sens. Environ. 114, 2048–2058. <https://doi.org/10.1016/j.rse.2010.04.011>.
- Hu, C., Lee, Z., Ma, R., Yu, K., Li, D., Shang, S., 2010b. Moderate Resolution Imaging Spectroradiometer (MODIS) observations of cyanobacteria blooms in Taihu Lake, China. J. Geophys. Res. Oceans 115 <https://doi.org/10.1029/2009jc005511>. (C04002).
- Hu, C., Li, D., Chen, C., Ge, J., Muller-Karger, F.E., Liu, J., Yu, F., He, M.-X., 2010c. On the recurrent *Ulva prolifera* blooms in the Yellow Sea and East China Sea. J. Geophys. Res. 115 <https://doi.org/10.1029/2009jc005561>. (C05017).
- Hu, S., Yang, H., Zhang, J., Chen, C., He, P., 2014. Small-scale early aggregation of green tide macroalgae observed on the Subei Bank, Yellow Sea. Mar. Pollut. Bull. 81, 166–173. <https://doi.org/10.1016/j.marpolbul.2014.02.001>.
- Hu, C., Feng, L., Hardy, R.F., Hochberg, E.J., 2015. Spectral and spatial requirements of remote measurements of pelagic *Sargassum* macroalgae. Remote Sens. Environ. <https://doi.org/10.1016/j.rse.2015.05.022>.
- Hu, C., Hardy, R., Ruder, E., Geggel, A., Feng, L., Powers, S., Hernandez, F., Graettinger, G., Bodnar, J., McDonald, T., 2016a. *Sargassum* coverage in the northeastern Gulf of Mexico during 2010 from Landsat and airborne observations: implications for the Deepwater Horizon oil spill impact assessment. Mar. Pollut. Bull. 107, 15–21. <https://doi.org/10.1016/j.marpolbul.2016.04.045>.
- Hu, C., Murch, B., Barnes, B.B., Wang, M., Maréchal, J.-P., Franks, J., Lapointe, B.E., Goodwin, D.S., Schell, J.M., Siuda, A.N., 2016b. *Sargassum* watch warns of incoming seaweed. EOS Trans. Am. Geophys. Union 97, 10–15. <https://doi.org/10.1029/2016EO058355>.
- Hu, L., Hu, C., He, M., 2017. Remote estimation of biomass of *Ulva prolifera* macroalgae in the Yellow Sea. Remote Sens. Environ. 192, 217–227. <https://doi.org/10.1016/j.rse.2017.01.037>.
- Huo, Y., Zhang, J., Chen, L., Hu, M., Yu, K., Chen, Q., He, Q., He, P., 2013. Green algae blooms caused by *Ulva prolifera* in the southern Yellow Sea: identification of the original bloom location and evaluation of biological processes occurring during the early northward floating period. Limnol. Oceanogr. 58, 2206–2218. <https://doi.org/10.4319/lo.2013.58.6.2206>.
- Keesing, J.K., Liu, D., Fearn, P., Garcia, R., 2011. Inter- and intra-annual patterns of *Ulva prolifera* green tides in the Yellow Sea during 2007–2009, their origin and relationship to the expansion of coastal seaweed aquaculture in China. Mar. Pollut. Bull. 62, 1169–1182. <https://doi.org/10.1016/j.marpolbul.2011.03.040>.
- Lee, J.H., Pang, I.-C., Moon, I.-J., Ryu, J.-H., 2011. On physical factors that controlled the massive green tide occurrence along the southern coast of the Shandong Peninsula in 2008: a numerical study using a particle-tracking experiment. J. Geophys. Res. 116 <https://doi.org/10.1029/2011jc007512>. (C12036).
- Leliaert, F., Zhang, X., Ye, N., Malta, E.-j., Engelen, A.H., Mineur, F., Verbruggen, H., De Clerck, O., 2009. Research note: identity of the Qingdao algal bloom. Phycol. Res. 57, 147–151. <https://doi.org/10.1111/j.1440-1835.2009.00532.x>.
- Liang, Q., Zhang, Y., Ma, R., Loisel, S., Li, J., Hu, M., 2017. A MODIS-based novel method to distinguish surface cyanobacterial scums and aquatic macrophytes in Lake Taihu. Remote Sens. 9, 133.
- Liu, D., Keesing, J.K., Xing, Q., Shi, P., 2009. World's largest macroalgal bloom caused by expansion of seaweed aquaculture in China. Mar. Pollut. Bull. 58, 888–895. <https://doi.org/10.1016/j.marpolbul.2009.01.013>.
- Liu, D., Keesing, J.K., Dong, Z., Zhen, Y., Di, B., Shi, Y., Fearn, P., Shi, P., 2010. Recurrence of the world's largest green-tide in 2009 in Yellow Sea, China: *Porphyra yezoensis* aquaculture rafts confirmed as nursery for macroalgal blooms. Mar. Pollut. Bull. 60, 1423–1432. <https://doi.org/10.1016/j.marpolbul.2010.05.015>.
- Liu, D., Keesing, J.K., He, P., Wang, Z., Shi, Y., Wang, Y., 2013. The world's largest macroalgal bloom in the Yellow Sea, China: formation and implications. Estuar. Coast. Shelf Sci. 129, 2–10. <https://doi.org/10.1016/j.ecss.2013.05.021>.
- Liu, F., Pang, S., Chopin, T., Gao, S., Shan, T., Zhao, X., Li, J., 2013. Understanding the recurrent large-scale green tide in the Yellow Sea: temporal and spatial correlations between multiple geographical, aquacultural and biological factors. Mar. Environ. Res. 83, 38–47. <https://doi.org/10.1016/j.marenvres.2012.10.007>.
- Liu, X., Li, Y., Wang, Z., Zhang, Q., Cai, X., 2015. Cruise observation of *Ulva prolifera* bloom in the southern Yellow Sea, China. Estuar. Coast. Shelf Sci. 163 (Part A), 17–22. <https://doi.org/10.1016/j.ecss.2014.09.014>.
- Liu, X., Wang, Z., Zhang, X., 2016. A review of the green tides in the Yellow Sea, China. Mar. Environ. Res. 119, 189–196. <https://doi.org/10.1016/j.marenvres.2016.06.004>.
- Lü, X., Qiao, F., 2008. Distribution of sunken macroalgae against the background of tidal circulation in the coastal waters of Qingdao, China, in summer 2008. Geophys. Res. Lett. 35. <https://doi.org/10.1029/2008GL036084>.
- Pang, S.J., Liu, F., Shan, T.F., Xu, N., Zhang, Z.H., Gao, S.Q., Chopin, T., Sun, S., 2010. Tracking the algal origin of the *Ulva* bloom in the Yellow Sea by a combination of molecular, morphological and physiological analyses. Mar. Environ. Res. 69, 207–215. <https://doi.org/10.1016/j.marenvres.2009.10.007>.
- Qi, L., Hu, C., Xing, Q., Shang, S., 2016. Long-term trend of *Ulva prolifera* blooms in the western Yellow Sea. Harmful Algae 58, 35–44. <https://doi.org/10.1016/j.hal.2016.07.004>.
- Shen, F., Zhou, Y., Peng, X., Chen, Y., 2014. Satellite multi-sensor mapping of suspended particulate matter in turbid estuarine and coastal ocean, China. Int. J. Remote Sens. 35, 4173–4192. <https://doi.org/10.1080/01431161.2014.916053>.
- Shi, W., Wang, M., 2009. Green macroalgae blooms in the Yellow Sea during the spring and summer of 2008. J. Geophys. Res. Oceans 114 <https://doi.org/10.1029/2009jc005513>. (C12010).
- Storey, J., Choate, M., Lee, K., 2014. Landsat 8 operational land imager on-orbit geometric calibration and performance. Remote Sens. 6, 11127–11152.
- Tan, B., Woodcock, C.E., Hu, J., Zhang, P., Ozdogan, M., Huang, D., Yang, W., Knyazikhin, Y., Myneni, R.B., 2006. The impact of gridding artifacts on the local spatial properties of MODIS data: implications for validation, compositing, and band-to-band registration across resolutions. Remote Sens. Environ. 105, 98–114. <https://doi.org/10.1016/j.rse.2006.06.008>.
- Thorhaug, A., Richardson, A.D., Berlyn, G.P., 2007. Spectral reflectance of the seagrasses: *Thalassia testudinum*, *Halodule wrightii*, *Syringodium filiforme* and five marine algae. Int. J. Remote Sens. 28, 1487–1501. <https://doi.org/10.1080/01431160600954662>.
- Tucker, C.J., 1979. Red and photographic infrared linear combinations for monitoring vegetation. Remote Sens. Environ. 8, 127–150. [https://doi.org/10.1016/0034-4257\(79\)90013-0](https://doi.org/10.1016/0034-4257(79)90013-0).
- Uptdike, T., Comp, C., 2010. Radiometric Use of WorldView-2 Imagery. Technical Note. DigitalGlobe Inc.
- Vahtmäe, E., Kotta, J., Orav-Kotta, H., Kotta, I., Pärnaja, M., Kutser, T., 2018. Predicting macroalgal pigments (chlorophyll a, chlorophyll b, chlorophyll a + b, carotenoids) in various environmental conditions using high-resolution hyperspectral spectroradiometers. Int. J. Remote Sens. 39, 5716–5738. <https://doi.org/10.1080/01431161.2017.1399481>.
- Vanhellemont, Q., Ruddick, K., 2014. Turbid wakes associated with offshore wind turbines observed with Landsat 8. Remote Sens. Environ. 145, 105–115. <https://doi.org/10.1016/j.rse.2014.01.009>.
- Vermote, E.F., Tanré, D., Deuzé, J.L., Herman, M., Morcrette, J.-J., 1997. Second simulation of the satellite signal in the solar spectrum, 6S: an overview. IEEE Trans. Geosci. Remote Sens. 35.
- Wang, M., Hu, C., 2016. Mapping and quantifying *Sargassum* distribution and coverage in the Central West Atlantic using MODIS observations. Remote Sens. Environ. 183, 350–367. <https://doi.org/10.1016/j.rse.2016.04.019>.
- Wang, W., Wang, F., Chen, S., Sun, X., Wang, X., Xing, S., Jun, W., 2008. PCR amplification and sequence analysis of ITS regions of *Enteromorpha prolifera* (in Chinese with English abstract). Mar. Fish. Res. 29, 124–129.
- Wang, Z., Xiao, J., Fan, S., Li, Y., Liu, X., Liu, D., 2015. Who made the world's largest green tide in China?—an integrated study on the initiation and early development of the green tide in Yellow Sea. Limnol. Oceanogr. 1–21. <https://doi.org/10.1002/lno.10083>.
- Wolfe, R.E., Roy, D.P., Vermote, E., 1998. MODIS land data storage, gridding, and compositing methodology: level 2 grid. IEEE Trans. Geosci. Remote Sens. 36, 1324–1338. <https://doi.org/10.1109/36.701082>.
- Xing, Q., Hu, C., 2016. Mapping macroalgal blooms in the Yellow Sea and East China Sea using HJ-1 and Landsat data: application of a virtual baseline reflectance height technique. Remote Sens. Environ. 178, 113–126. <https://doi.org/10.1016/j.rse.2016.02.065>.
- Xing, Q., Tosi, L., Braga, F., Gao, X., Gao, M., 2015. Interpreting the progressive eutrophication behind the world's largest macroalgal blooms with water quality and ocean color data. Nat. Hazards 78, 7–21. <https://doi.org/10.1007/s11069-015-1694-x>.
- Xu, Q., Zhang, H., Ju, L., Chen, M., 2014a. Interannual variability of *Ulva prolifera* blooms in the Yellow Sea. Int. J. Remote Sens. 35, 4099–4113. <https://doi.org/10.1080/01431161.2014.916052>.
- Xu, W., Gong, J., Wang, M., 2014b. Development, application, and prospects for Chinese land observation satellites. Geo-spatial Inf. Sci. 17, 102–109. <https://doi.org/10.1080/10095020.2014.917454>.
- Xu, Q., Zhang, H., Cheng, Y., 2016. Multi-sensor monitoring of *Ulva prolifera* blooms in the Yellow Sea using different methods. Front. Earth Sci. 10, 378–388. <https://doi.org/10.1007/s11707-015-0528-1>.
- Zhang, X., Mao, Y., Zhuang, Z., Liu, S., Qingyin, W., Naihao, Y., 2008. Morphological characteristics and molecular phylogenetic analysis of green tide *Enteromorpha* sp. occurred in the Yellow Sea (in Chinese with English abstract). J. Fish. China 15, 822–829.
- Zhang, J., Huo, Y., Yu, K., Chen, Q., He, Q., Han, W., Chen, L., Cao, J., Shi, D., He, P., 2013. Growth characteristics and reproductive capability of green tide algae in Rudong coast, China. J. Appl. Phycol. 25, 795–803. <https://doi.org/10.1007/s10811-012-9972-4>.
- Zhang, Y., Ma, R., Duan, H., Loisel, A.L., Xu, J., Ma, M., 2014. A novel algorithm to estimate algal bloom coverage to subpixel resolution in Lake Taihu. IEEE J. Sel. Top. Appl. Earth Obs. Remote Sens. 7, 3060–3068. <https://doi.org/10.1109/JSTARS.2014.2327076>.
- Zhang, J., Zhao, P., Huo, Y., Yu, K., He, P., 2017. The fast expansion of *Pyropia* aquaculture in “Sansha” regions should be mainly responsible for the *Ulva* blooms in Yellow Sea. Estuar. Coast. Shelf Sci. 189, 58–65. <https://doi.org/10.1016/j.ecss.2017.03.011>.
- Zhong, S., Ding, Y., Li, Z., Liu, A., Tong, Z., Wang, Q., 2013. Error analysis on *Enteromorpha prolifera* monitoring using MODIS data (in Chinese with English abstract). Remote Sens. Inf. 28, 38–42.